

www.acsami.org Research Article

## Three-Dimensional Printing of Ceramics through "Carving" a Gel and "Filling in" the Precursor Polymer

Mohammadreza Mahmoudi, Chao Wang, Salvador Moreno, Scott R. Burlison, Diana Alatalo, Fatemeh Hassanipour, Samantha E. Smith, Mohammad Naraghi, and Majid Minary - Jolandan\*



Cite This: ACS Appl. Mater. Interfaces 2020, 12, 31984-31991



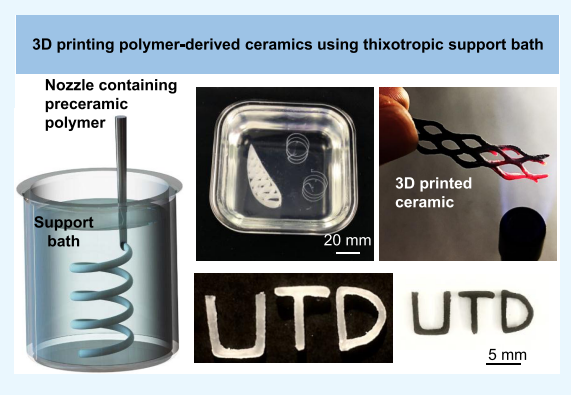
**ACCESS** 

Metrics & More

Article Recommendations

s Supporting Information

ABSTRACT: Achieving a viable process for three-dimensional (3D) printing of ceramics is a sought-after goal in a wide range of fields including electronics and sensors for harsh environments, microelectromechanical devices, energy storage materials, and structural materials, among others. Low laser absorption of ceramic powders renders available additive manufacturing (AM) technologies for metals not suitable for ceramics. Polymer solutions that can be converted to ceramics (preceramic polymers) offer a unique opportunity to 3D-print ceramics; however, due to the low viscosity of these polymers, so far, their 3D printing has only been possible by combining them with specialized light-sensitive agents and subsequently cross-linking them layer by layer by rastering an optical beam. The slow rate, lack of scalability to large specimens, and specialized chemistry requirements of this optical process are fundamental limitations. Here, we demonstrate



3D printing of ceramics enabled by dispensing the preceramic polymer at the tip of a moving nozzle into a gel that can reversibly switch between fluid and solid states, and subsequently thermally cross-linking the entire printed part "at-once" while still inside the same gel. The solid gel, which is composed of mineral oil and silica nanoparticles, converts to fluid at the tip of the moving nozzle, allows the polymer solution to be dispensed, and quickly returns to a solid state to maintain the geometry of the printed polymer both during printing and the subsequent high-temperature ( $160\,^{\circ}$ C) cross-linking. We retrieve the cross-linked part from the gel and convert it to ceramic by high-temperature pyrolysis. This scalable process opens up new opportunities for low-cost and high-speed production of complex three-dimensional ceramic parts and will be widely used for high temperature and corrosive environment applications, including electronics and sensors, microelectromechanical systems, energy and structural applications.

KEYWORDS: ceramic 3D printing, polymer-derived ceramics (PDCs), preceramic polymers, solidlike liquid gels, pyrolysis

#### **■** INTRODUCTION

Scientists across several fields including electronics and sensors for harsh environments, microelectromechanical devices, energy storage materials, and structural materials are interested in a viable process for three-dimensional (3D) printing of ceramics. This is because of several factors: the traditional method of ceramic manufacturing based on powder consolidation and sintering is costly, casting and machining ceramics is nontrivial as opposed to metals and polymers; additionally, the extremely high melting point of most ceramics, in addition to their low laser absorption, renders available additive manufacturing (AM) technologies for metals nonapplicable to or not suitable for ceramics.

Various methods for AM of ceramics have been reported such as photolithography, binder jetting, and laser sintering. The photolithography process involves selective curing of a photosensitive resin containing ceramic particles.<sup>3,4</sup> In the binder jetting process, a liquid binder agent is selectively deposited onto ceramic particles.<sup>5</sup> In the laser sintering process, ceramic powder is selectively fused using a laser

beam.<sup>6,7</sup> These processes are all layer-by-layer, powder-based, and face several challenges such as porosity after removal of the binder or resin, which makes the consolidation step to achieve a dense 3D-printed part difficult. Most ceramics have low laser absorption, which makes laser-based processes challenging. In addition, laser-based processes generate a large thermal gradient in the 3D-printed part, which is the driving force for crack formation. Porosity and cracks in 3D-printed ceramics result in low strength. These processes are often slow and require a binder removal post processing step. Freeform extrusion of ceramic particle-based slurries is another method for AM of ceramics.<sup>8</sup> This process prints a composite

Received: May 5, 2020 Accepted: June 17, 2020 Published: June 17, 2020





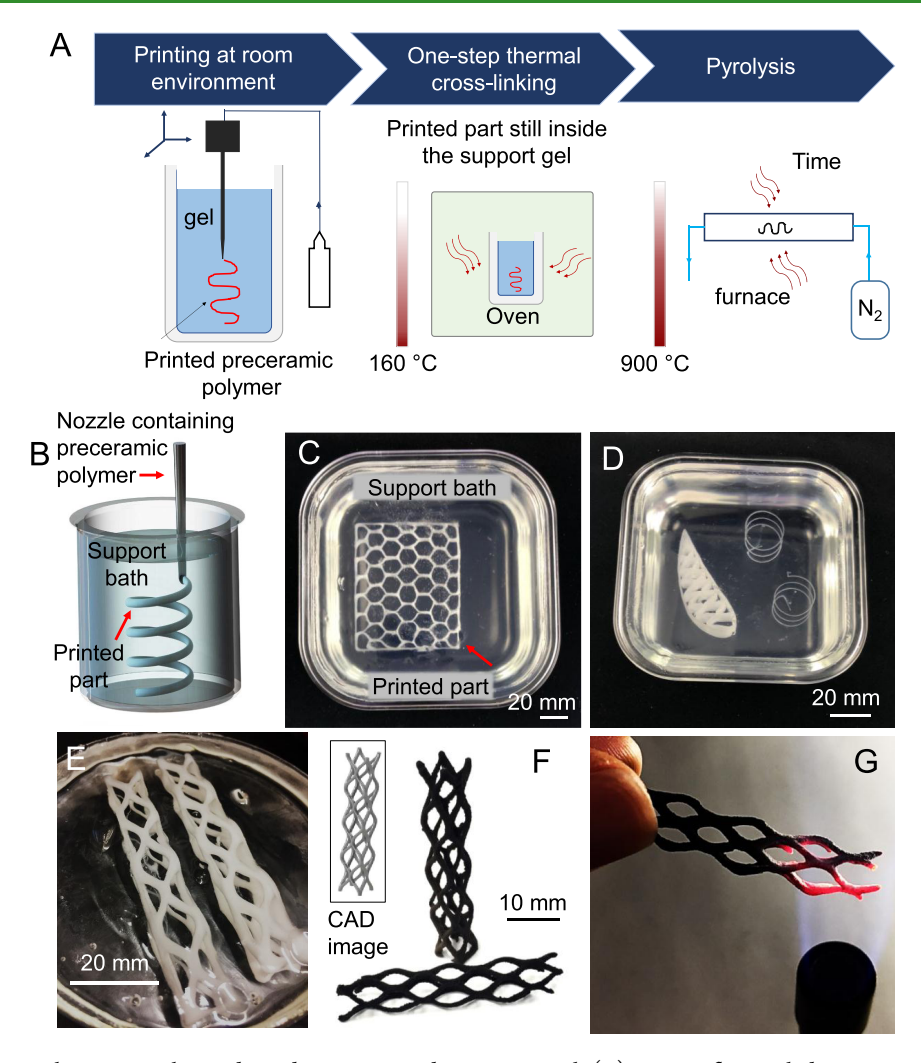


Figure 1. Three-dimensional-printing polymer-derived ceramics inside a support gel. (A) Process flow including printing a preceramic polymer inside the support gel and "one-step" cross-linking, while the printed part is still inside the gel, followed by retrieval of the cross-linked polymer from the gel and pyrolysis inside the furnace. (B) Schematic shows a close-up view of the polymer dispensing from the nozzle tip into the gel. (C)—(E) Photos of the several printed geometries including a honeycomb, an airfoil, two helical springs, and two truss-beams inside the gel. (F) CAD image and photo of the truss-beam structure after pyrolysis. (G) Final printed specimen shown over a flame with  $T \sim 1400$  °C. The change in the sample weight was  $\sim$ 0.6% for 2 min hold on the flame.

of a binder and ceramic particles and requires binder removal post-processing, which often leaves behind a porous structure.

The polymer-derived ceramics (PDCs), a class of ceramics that are obtained by pyrolysis of polymer precursors, lend themselves to AM processes. This is because in their polymer state they are suitable for shaping such as printing, and the subsequent cross-linking locks the printed geometry. 10-12 PDCs were introduced in the 1960s and include SiC, SiOC, Si<sub>3</sub>N<sub>4</sub>, BN, AlN, SiCN, BCN, among others. PDCs are mostly used for the infiltration of ceramic matrix composites and ceramic fiber synthesis. In addition, their electrical conductivity, luminescence, and piezoresistivity make them attractive for functional applications. 13 By having Si-rich and C-rich nanosized domains, PDCs are stable against creep, oxidation, crystallization, or phase separation up to 1500 °C or higher temperature. The pyrolysis temperature of PDCs is in the range of 1000-1300 °C, which is lower than temperatures (>1600 °C) typically used in classic ceramic powder-based

Layer-by-layer, selective curing of a photosensitive slurry via a dynamic mask exposure was reported for AM of dense alumina ceramics by Schwentenwein et al. 14 This process uses a photocurable ceramic suspension comprises high-purity alumina powder dispersed in a light-sensitive organic matrix. The organic matrix consists of a photoinitiator, monomers based on methacrylate chemistry, and additives. After the debinding and sintering process, the printed parts showed a density corresponding to 99.3% of the theoretical density of alumina, which is an indication of excellent densification. In 2015, Zanchetta et al. reported layer-by-layer stereolithography of SiOC ceramic microcomponents using an engineered photosensitive methyl-silsesquioxane preceramic polymer. 13 This report was the first direct fabrication of 3D highperformance ceramics from preceramic polysiloxanes with high ceramic yield. The engineered preceramic precursor started from a commercially available silicone (SILRES MK) and an organically modified silicon alkoxide 3-(trimethoxysilyl) propyl methacrylate. In 2015, Eckel et al. reported AM of PDCs via stereolithography (SLA) and self-propagating photopolymerization techniques. 15 Ultraviolet (UV)-active preceramic monomers were obtained by the incorporation of UV-sensitive side groups (photoinitiators) to the backbone of the precursor

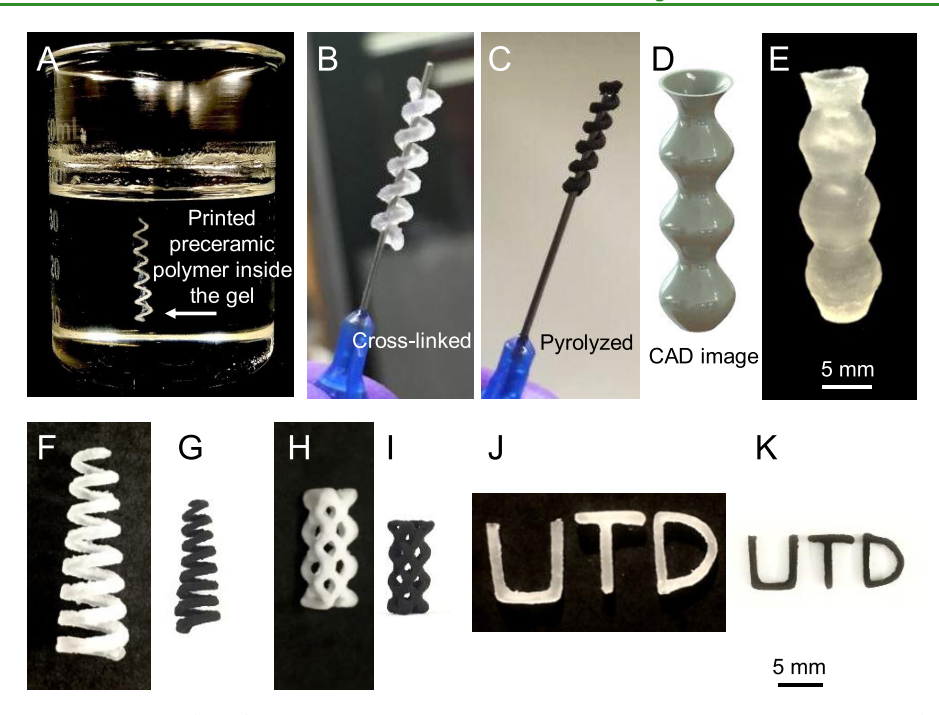


Figure 2. Sample 3D-printed geometries. (A–C) Helix inside the gel, after cross-linking and after pyrolysis, respectively. (D, E) CAD image and a photo of a printed hollow vase, (F)-(J) cross-linked, and (G)-(K) pyrolyzed samples. Printing durations for the parts ranged within  $\sim$ 8–115 s (provided in Table S1).

polymer. Cross-linked polymer patterns were generated by scanning using a UV beam, which were subsequently postcured by thermal treatment or additional UV exposure. The printed and cured polymer was pyrolyzed to obtain virtually pore-free solid ceramic parts. The unpolymerized resin was recycled and reused. These processes based on photosensitive slurry or UVsensitive resin require specialized chemistry. Additionally, SLA is rather slow since at each scan  $30-100 \mu m$  slices are built. The ridges generated from the layer-by-layer scanning process on the surface of the printed ceramic part are surface flaws and may result in stress concentrations, which is detrimental for ceramics given their low fracture toughness. On the other hand, self-propagating photopolymerization is limited to structures with linear features extending from the exposure surface (such as lattices and honeycombs). Recently, 3D nanofabrication of SiOC ceramic structures using two-photon lithography (2PL) with an engineered printing configuration by starting from a selected preceramic formulation was demonstrated to achieve 3D complex architectures with a size on the order of 100  $\mu$ m in the z-direction, with 450 nm resolution.16

Here, we report on a new approach for high-speed 3D printing of PDCs that does not require UV or photocuring or rheology modifiers and results in binder-free printed parts. In this process, the 3D-printed precursor ceramic polymer is thermally cured in a single step at the end of the printing process, as opposed to layer-by-layer curing. In recent studies, 3D printing of polymers with the aid of a viscoplastic liquid sacrificial support has emerged as a viable method to generate spatially structured soft matters. This method relies on controllable interactions between two liquids, the precursor of the main structure (such as a resin) and the liquid support bath. While the former can be considered as a Newtonian fluid, the latter is a so-called "yield stress fluid," which switches reversibly from a semisolid to a liquid when subjected to sufficiently high shear stress to allow for extrusion of the liquid

precursor, and retains the printed part shape in the wake of the nozzle when shear stress is removed. In this printing process, the shear stress is provided by the nozzle motion. The liquid precursor is then cured inside the support bath and retrieved for subsequent processing steps. While printing in yield stress fluids has been used for biological systems and soft materials that can be cured at low temperatures,  $^{17-19}$  PDCs require thermally induced curing at elevated temperatures (>120 °C) and are much more sensitive to surface defects compared to biological materials. We report AM of SiOC (silicon oxycarbide) ceramics in a yield stress fluid support bath that is based on mineral oil and silica nanoparticles, which makes it suitable for high-temperature curing required for SiOC, and can further be applied to other PDC types including SiC, SiCN, and Si<sub>3</sub>N<sub>4</sub>.

#### ■ RESULTS AND DISCUSSION

The schematic in Figure 1A shows the overall process flow, which includes printing the preceramic polymer inside the support bath at room environment, cross-linking the printed part while still inside the support bath in an oven at temperature  $\sim\!160\,^{\circ}\mathrm{C}$ , followed by retrieval of the cured specimen, and finally pyrolysis in a furnace at  $\sim\!900\,^{\circ}\mathrm{C}$  (see Movie S1). The magnified view of the nozzle and bath is shown in Figure 1B. The in-house designed printer consists of an injection system that controls the flow rate of the precursor polymer solution and a delta-type XYZ positioning system. The trajectory and nozzle translational speed are controlled by G-code.

We designed a yield stress support bath that can sustain its required rheological properties to support the printed geometry both at the room environment and at the temperature required for cross-linking (~160 °C). This temperature limit excludes aqueous yield stress bath due to water boiling, which will break up printed parts. Details of the materials for the bath and the preceramic polymer solution are

presented in the Materials and Methods section. The support bath is composed of mineral oil and silica nanoparticles. The silica nanoparticles are rheology modifiers in this bath, given their network structure. Pure mineral oil does not have the required property to switch between the solid and fluid states, without the addition of silica nanoparticles. The capability of switching between the solid and liquid states is the key in this 3D printing process, since otherwise the printed preceramic polymer cannot be extruded or its shape cannot be maintained. The reported bath composition was determined by an iterative process. Rheological properties of the supporting bath were tuned by changing the volume fraction of the silica nanoparticles. Increasing the volume fraction of the fumed silica in the suspension led to the formation of sol, pregel, and gel. One important consideration in this process was to avoid gravitational instability, which required the support bath to be viscous enough to keep the preceramic polymer in the desired shape and to be stable during the cross-linking at a higher temperature. The rheological properties of the bath are discussed later in the manuscript. The thermogravimetric analysis confirmed that the oil bath was stable up to ~200 °C (the boiling point of the mineral oil is  $\sim$ 310 °C).

Figure 1C–E shows photos of the several printed geometries including a honeycomb, an airfoil, two helical springs, and two truss-beams inside the gel. One advantage of this bath is its transparency, such that the printing process can be monitored in situ. After curing, printed parts are readily retrieved from the support bath and rinsed with running ethanol for subsequent processing. Figure 1F shows the truss-beams after pyrolysis. During pyrolysis at ~900 °C in a nitrogen environment, polymer-to-ceramic transformation occurs. The polymer-toceramic transformation is accompanied by the release of volatile species (CH<sub>4</sub>, H<sub>2</sub>, CO<sub>2</sub>, H<sub>2</sub>O, and hydrocarbons) and results in shrinkage in the dimensions of the printed part, which is typical of all preceramic polymers. The linear shrinkage percentage was estimated, by image analysis of before and after pyrolysis, to be ~15%. Figure 1G shows a pyrolyzed part held over a flame, which demonstrates potential application of the process to print structures for the harsh environment. The temperature of the flames was  $\sim$ 1400 °C. The change in the sample weight was  $\sim 0.6\%$  for 2 min hold on the flame.

Figure 2 shows several 3D-printed geometries after curing and pyrolysis. These samples include a helix, a hollow vase, a cone helix, a 3D grid structure, and "UTD" letters. The printing durations for these parts are provided in Table S1, which range from  $\sim 8$  to 115 s, showing the rapid printing speed of the process. Subsequent curing and pyrolysis can be done at once for all parts.

The inset in Figure 3A shows the preceramic polymer in a vial. The viscosity of the polymer is  $\sim$ 790 cP (1 cP =  $10^{-3}$  Pa.s). In Figure 3A, this viscosity is compared to other fluids such as engine oil and honey to show the rather low viscosity of the preceramic polymer. As an example, the preceramic polymer solution is more than 13 times less viscous than honey. The polymer solution used in this study does not contain any rheology modifiers or additives as opposed to all other previously reported methods for such low-viscosity polymers. <sup>13,20</sup> Due to its low viscosity, it cannot be directly extruded without support, as it cannot maintain its shape. As such the two most common methods for 3D printing of preceramic polymers are using layer-by-layer photocuring and mixing with other additives and rheology modifiers to increase

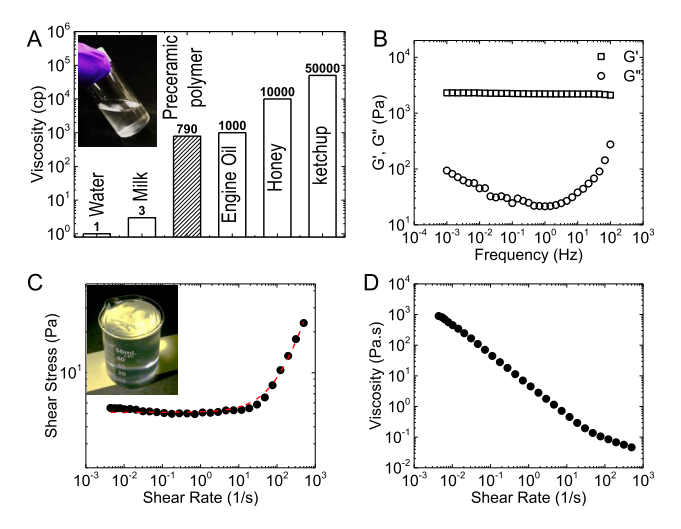


**Figure 3.** Rheological properties of the preceramic polymer and the support gel. (A) Comparison of the preceramic polymer viscosity to other common liquids. The inset shows a bottle of the ceramic polymer solution. (B–D) Rheological properties of the support gel (B) storage and loss moduli vs frequency; (C) shear stress vs shear rate; and (D) viscosity vs shear rate. The inset in C shows a container of the support gel (1 cP =  $10^{-3}$  Pa.s).

the viscosity. We note that the interfacial tension and other rheological properties of the preceramic polymer and bath are important in the 3D- printing process. In this work, we used commercially available preceramic polymer, without changing the chemistry or composition. The properties of the preceramic polymer during the printing process are not controlled, and the polymer is physically extruded through the nozzle and dispensed into the bath. The support bath is shown in the inset in Figure 3C. It is transparent and free of any visible bubbles. When held upside down, the gel holds its shape without flowing, which shows its solidlike behavior in the absence of shear stress.

Figure 3B-D shows the rheological properties of the support bath. As mentioned above, the support bath was prepared by adding silica nanoparticles (with an average size of  $\sim$ 200-300 nm) to the mineral oil to form a yield stress fluid. An ideal support bath should have characteristics of a solid to support the printed structure (during printing and also during thermal curing), as well as the characteristics of a fluid to enable nozzle movement with different speeds with minimal resistance. The yield stress fluid here serves as a support material that switches reversibly from a solid to a liquid when subjected to sufficiently high shear stress. During printing, the shear stress is provided by the nozzle motion. In the vicinity of the nozzle, the liquid phase precursor polymer is dispensed from the nozzle. In the wake of the nozzle, the bath is designed to turn into a "solid" state (after removal of the nozzle shear stress), maintaining the shape of the liquid precursor.

Figure 3B shows the storage modulus (G') and the loss modulus (G'') vs frequency for the bath. G' vs frequency remains flat and separated from the G'', which is a characteristic of soft elastic solids with damping. The shear stress vs shear rate shows a plateau for low shear rate  $(< \sim 10 \text{ s}^{-1})$  (Figure 3C), which corresponds to the yield stress of the bath. For stress above this yield stress, the bath fluidizes or behaves like a fluid. The plateau region corresponds to shear rate independent stress dominated by elasticity. When the bath fluidizes for shear rate larger than the plateau region, its

behavior is dominated by viscous loss. The Herschel–Bulkley model is commonly used to describe the behavior of yield stress fluids:  $\sigma = \sigma_y + k\dot{\gamma}^n$ , in which  $\sigma_y$  is the yield stress, k is the consistency factor, and n is the flow index. For shear-thinning fluids, n < 1. Based on this model fitted to the data in Figure 3C, the yield stress of the bath is  $\sim 5.1$  Pa, and the flow index and the consistency factors are 0.9 and 0.05, respectively. Given the low-yield stress of the bath compared to the hydrostatic pressure at reasonable bath depth  $(\rho gh)$ , there is no concern of static crevasse formation, since the hydrostatic pressure easily refills the fluid behind the nozzle. This is important to prevent the flow of the preceramic polymer into this space, which will result in skewed printing geometries. The support bath gel composition can be tuned by changing the silica nanoparticle concentration and the mineral oil type.

Figure 3D shows the apparent steady-state shear viscosity of the support bath calculated from the ratio of the steady-state shear stress and shear rate. The response shows a shear-thinning behavior. The viscosity decreases from  $\sim 10^3$  Pa·s to  $< 10^{-1}$  Pa.s over a shear rate range of  $4 \times 10^{-3}$  to  $500 \text{ s}^{-1}$ .

In this work, we used commercially available preceramic polymers, without changing the chemistry or composition. We note that the rheological properties of the bath and the preceramic polymer, the interfacial tension between the preceramic polymer and the bath, as well as the printing rate (nozzle travel speed), and the flow rate of the preceramic polymer in the nozzle overall determine the resolution and precision of the printing process. The cross-sectional area (A)of the extruded polymer from the nozzle is mostly determined by the flow rate (Q) and the travel velocity (V) of the nozzle (A = O/V). The flow rate is controlled by a syringe pump. For these experiments, a flow rate of ~ 1 mL/min with a nozzle speed of ~15 mm/s was used. This results in a cross-sectional area of ~1.1 mm<sup>2</sup>, which assuming a circular cross section yields a diameter of  $d \sim 1.2$  mm. The diameter of the nozzle was ~0.6 mm. To prevent transient recirculating wake behind the nozzle, which can intermix the support bath material and the preceramic polymer, the nozzle speed must be kept below  $V \sim \frac{\rho g L d}{r}$ , in which  $\rho$  is the density of the bath, L is the nozzle length immersed in the bath, d is the nozzle diameter, and  $\eta$  is the bath viscosity.<sup>21</sup> In our experiment, the nozzle speed was well below the critical speed that would cause recirculating wake ( $\sim$ 250 mm/s).

density mismatch  $(\Delta \rho)$  between the support bath and the preceramic polymer solution may result in the sink or rise of the printed structures in the bath. For a sphere with diameter d, the rise/sink speed  $(V_{\rm rs})$  can be found using  $V_{\rm rs} \sim \frac{\Delta \rho_{\rm g} d^2}{18\eta}.^{2.1}$ Assuming a spherical geometry with the typical print crosssectional area in this work ( $\sim$ 1.2 mm), the sinking speed is estimated to be ~0.096 mm/s, which is rather small considering to the total printing duration. Given that the viscosity of the support bath depends on the shear rate (Figure 3D), in this calculation, a viscosity under the printing shear rate (~2 Pa·s) was used. In the absence of shear stress, the viscosity of the bath is more than 103 Pa·s, and hence the sinking speed would be nearly zero, as expected for solid behavior of the bath. Obvious sinking or rising of the printed object in the support bath was not observed during printing or after curing. The minimum stable feature size  $(I_c)$  to prevent the Rayleigh instability that will cause break up of the printed

The instability caused by gravitational forces that result from

preceramic polymer in the bath can be estimated using  $I_{\rm c}=\frac{\gamma_{\rm oil-polymer}}{\sigma_{\rm y}},^{21}$  in which  $\gamma_{\rm oil-polymer}$  is the interfacial tension

between the bath and the preceramic polymer solution and  $\sigma_y$  is the yield stress of the bath ( $\sim$ 5.1 Pa). However, the smallest stable feature size in our work was  $\sim$ 0.7 mm, without break up of the printed polymer, and this is more attributed to the limitations of the printer and not the process itself.

The thermogravimetric analysis (TGA/DTG) combined with differential scanning calorimetry (DSC) was used to obtain insight into the thermally induced chemical changes of the material during processing. The thermal analysis (TGA/DSC/DTG) was conducted at a heating rate of 20 °C/min under a flowing  $N_2$  atmosphere (see Figure 4A,B). According

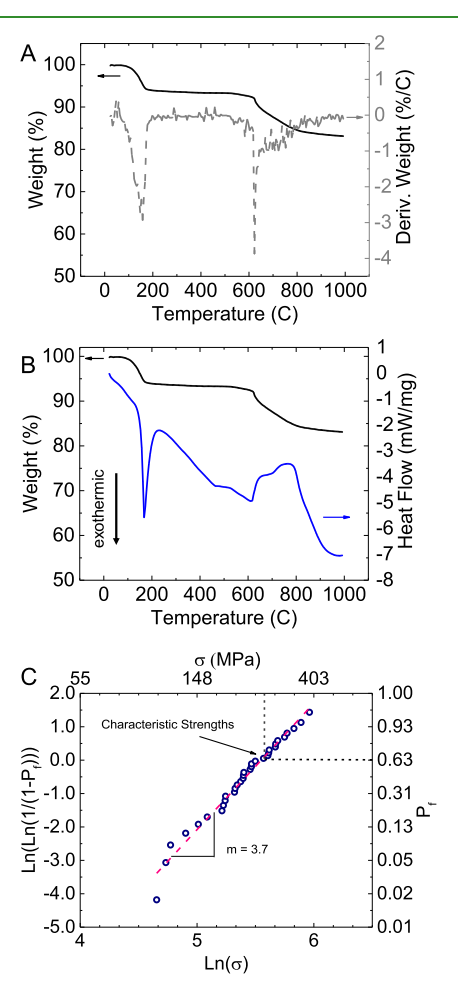


**Figure 4.** Thermal and mechanical properties. (A) Thermogravimetric analysis (TGA/DTG) response and (B) differential scanning calorimetry (DSC) response for the preceramic polymer. (C) Weibull plot for the strength of 3D-printed ceramic. n = 33.

to thermal analysis experiments, the total mass loss of the preceramic polymer during ceramization (the process of turning into a ceramic) up to 1000 °C was 16.4%. The thermally driven chemical cross-linking and pyrolysis lead to the observed mass loss through outgassing, which is also accompanied by material consolidation. The majority of the observed mass loss occurs at temperatures below 700 °C mainly within two temperature ranges. The first major mass loss occurs between 127 and 233 °C (by  $\sim$ 2.9%, the peak rate at  $\sim$ 158 °C). This mass loss is accompanied by a strong

exothermic peak at ~168 °C in the DSC spectra. This mass loss is attributed to chemical cross-linking during which the precursor is transformed into an infusible organic/inorganic molecular network. Generally, hydrosilylation, hydrolysis, and condensation reactions are involved in the cross-linking stage of polymer-derived ceramics. The cross-linking is crucial to the formation of a 3D structure of ceramic at higher heat treatment temperatures as it prevents the melting of the material during later stages. The cross-linking process also increases the ceramic yield since it prevents the loss and fragmentation of low-molecular-weight components of the precursor. In this work, cross-linking was achieved using dicumyl peroxide.<sup>23</sup> The second major mass loss occurs in the temperature range of 593–933 °C (by an additional  $\sim$ 3.9%, the peak rate at  $\sim$ 623 °C). Ceramization happens within this temperature range. Considerable bond cleavages and redistribution reactions between Si-H, Si-C, and Si-O occurs in this temperature range.<sup>23,24</sup> The broad endothermic peak observed in the DSC response at this temperature range represents the energy intake for bonds cleavage. The mass loss in this temperature range is due to the formation of a variety of hydrocarbons such as CH<sub>4</sub> and hydrogen, which are released from the material.<sup>23</sup> As a result of the cross-linking and pyrolysis reactions, the ceramic material consisting of an amorphous SiOC network and free carbon (turbostratic domains) forms. Various catalysts can be used for cross-linking of the preceramic polymer. Type and the content of the added catalyst can affect the cross-linking process. This is because the cross-linking helps to preserve the precursor components with lower-molecular-weight during the ceramization step. <sup>23</sup> According to the recommendation of the supplier (Starfire), we used dicumyl peroxide as the catalyst. The mass loss of 16.4% in this experiment is much lower than the previous study (30%) by Kulkarni on the same polymer (SPR-036), in which 100 mL/g of the Pt catalyst was used.<sup>25</sup> Different mass loss ratios for the same precursor type can be attributed to different degrees of cross-linking during the early stages of heat treatment, as mediated for instance by the catalyst content.

Based on the thermal analysis results, a pyrolysis temperature—time profile was designed (Figure S1). The mass loss during ceramization is due to the release of gasses from the precursor polymer. Rapid heat-up during the ceramization may lead to the formation of defects and large pores. Hence, the heating rate in the temperature range of 450–900 °C was chosen to be several times slower than the initial rate. The pyrolysis temperature—time cycle was as follows: from room temperature to 450 °C at a heating rate of 2 °C/min, and from 450 to 900 °C at a heating rate of 0.5 °C/min, followed by a hold at 900 °C for 1 h.

A separate thermal analysis was conducted on the support bath, and cross-linked cast preceramic (as opposed to 3D-printed inside a support bath) and cross-linked 3D-printed preceramic. Details of this analysis are given in the Supporting Information in Figure S2. The difference in the mass change between the cast and printed samples shows that even after rinsing with ethanol, a layer of mineral oil and silica nanoparticles remained on the surface of the printed parts. As it is shown in the TGA response of the bath (Figure S2), the mineral oil almost entirely evaporates during pyrolysis, leaving behind the condensed silica nanoparticles that coat the surface of the pyrolyzed specimens. This is also confirmed by scanning electron microscopic (SEM) images and energy-

dispersive spectrometry (EDS) analysis in Figures S4 and S5 and Table S2.

The mechanical properties of the pyrolyzed 3D-printed ceramic were obtained by three-point flexure (bending) experiment. Details of the specimen preparation and testing procedure are presented in the Materials and Method section. For ceramics, the three-point bending test is preferred to the commonly used compression test.<sup>26–28</sup> This is because the compression test tends to close the processing flaws (such as microcrack and pores) in the material. However, during real-life applications, these processing flaws can be subjected to tensile loading. The compression test for ceramics does not truly examine such mechanical properties. A total of 33 3D-printed specimens were prepared according to the ASTM standard (C1684-18).<sup>29</sup>

Figure S3 shows a photograph of the ceramic beam under a three-point bending experiment mounted on a microtensile tester. Figure S4 shows SEM images of typical fracture surfaces of the ceramic. Brittle nature of the fracture can be observed in the smooth and "shiny" surfaces.

For the 3D-printed specimens, we obtained a strength of  $232 \pm 69$  MPa (n=33). For ceramic materials, the ASTM standard<sup>30</sup> calls reporting statistical data based on Weibull distribution parameters. This is because the mechanical properties of the brittle materials largely depend on the distribution of flaws, and hence, deterministic approaches to analyze the data from the experiments are not comprehensive. The strength of the ceramic under three-point bending is expressed in terms of two-parameter Weibull distribution, as

shown in Figure 4C, 
$$P_{\rm f}=1-\exp\left(-\frac{\sigma}{\sigma_0}\right)^m$$
. <sup>31</sup> Such analysis considers the variability in the ceramic strength as a function of flaw population in the material. <sup>32</sup>  $m$  is the Weibull modulus, and  $\sigma_0$  is the characteristic strength. The Weibull modulus is the shape parameter that maps a failure probability of a

specimen in a range of stress. Specimens' flexural strengths were ranked in ascending order and assigned a probability using  $P_{\rm f}=(i-0.5)/n$ , where n is the total number of specimens. Probabilities and the flexural strengths are presented in terms of  $\ln(\ln(1/1-P_{\rm f}))$  and  $\ln(\sigma)$ . Based on this analysis, the characteristic strength, which is the value of stress for  $P_{\rm f}=63.2\%$ , for the 3D-printed ceramics was calculated to be ~257 MPa. The linear regression of the flexural strength yields the Weibull modulus of m=3.7 for 3D-printed specimens.

The mechanical properties of the ceramics largely depend on the specimen geometry and different processing used, and as such comparison of absolute values with other processes may not be straightforward. For example, specimens made in the thin-film form show larger characteristic strength given their small dimension and consequently smaller probability of flaws. We estimated the thickness of the residual silica particles to be  $\sim$ 115  $\mu$ m (Supporting Information). We do expect that this coating to affect the mechanical properties of the specimens, although marginal. This is given its small thickness (~10% of the specimen diameter), and also given that silica has comparable mechanical properties to the polymer-derived ceramic (SiOC). Although in this article we did not attempt to do so, this residual silica layer can be polished from the surface of the printed parts, if the measurement of absolute mechanical properties is intended. For example, a large part can be printed, then the silica coating can be polished, and finally specimens

can be cut from the polished material for mechanical property measurements.

#### CONCLUSIONS

We presented a new process for the additive manufacturing of polymer-derived ceramics using a thixotropic support bath. After printing and cross-linking in the same bath, the printed parts are retrieved from the bath and pyrolyzed to the final ceramic part. The one-step curing process after the printing process is advantageous for mechanical properties since nointerlayer interfaces are generated in the process. Although we focused on SiOC in this work, the process can be readily extended to other preceramic polymers. There are many different types of preceramic polymers such as SiOC, SiC, SiCN, SiBCN, among others. The preceramic polymer functions as the precursor to the final ceramic, after it goes through cross-linking and pyrolysis. The properties of the final ceramic depend on the composition and properties of the preceramic polymer. The process can also be easily extended to ceramic composites by adding chopped ceramic fibers and/ or functional nanoparticles. In this work, we focused on printing lab-scale components, this process can be readily scaled up. The support gel is made of low-cost and commercially available mineral oil and silica nanoparticles. A large container of the bath can be easily prepared. The nozzle size can be varied to obtain components with smaller or larger sizes as required. Larger ovens and furnaces can be used for curing and pyrolysis steps.

#### MATERIALS AND METHODS

Support Bath Preparation. The support bath was prepared by mixing 5 wt % fumed silica with an average particle size in the range of ~200−300 nm (Sigma Aldrich) in 95 wt % light mineral oil (VWR). The bath was hand-mixed until it turned into a clear gel. The air bubbles generated by mixing in the support bath were removed by exposing the bath to 2 h vacuum followed by resting at room temperature for 24 h.

**Preceramic Polymer Solution Preparation.** A solution was prepared by mixing dicumyl peroxide (Sigma Aldrich) and toluene (Fisher Chemical) at 1:1 ratio. The solution was stirred for at least 2 min using a vortex mixer until all dicumyl peroxide particles completely dissolved in toluene. This solution was added to Polyramic SPR-036 (Starfire Systems) at 2:98 wt % ratio. The solution was homogenously mixed using a magnetic stirrer for 5 min at 400 rpm. To prevent bubble formation during the curing process, the preceramic polymer solution was placed inside vacuum for 2 h.

Ceramic 3D Printing in Support Bath. Three-dimensional printing was performed using a delta-type 3D printer designed and built at UTD. The preceramic polymer solution was loaded into a syringe and injected by a NE-300 Just Infusion syringe pump. A sharp needle with an inner diameter of 0.024 inch was used as the nozzle. The nozzle motion was controlled via custom-written script functions and trajectory files. After printing, the precursor polymer was cured thermally at ~160 °C for 2 h inside the same bath. After curing, the printed parts were readily retrieved from the bath. The parts were rinsed with running ethanol before pyrolysis. The pyrolysis process was performed using a tube furnace (Thermo Scientific Lindberg/Blue M Mini-Mite) inside a nitrogen gas environment. The pyrolysis time—temperature cycle was as following: room temperature to 450 °C at 2 °C/min heating rate, 450—900 °C at 0.5 °C/min heating rate, followed by hold at 900 °C for 1 h.

Measurement of Rheological Properties. The rheological measurements were performed using an Anton Paar rheometer using a 50 mm cone with an apex angle of  $0.5^{\circ}$  and a 50 mm diameter bottom plate. Frequency sweeps were taken at 1% strain from  $10^{-3}$  to  $10^{2}$  Hz. The yield stress of the material was determined by applying a

shear rate sweep from  $4 \times 10^{-3}$  to  $500 \text{ s}^{-1}$ . The viscosity value for the preceramic polymer solution was obtained from the vendor (Starfire Systems).

**Mechanical Characterization.** The three-point flexural tests were performed using an MTI/Fullam SEMTester (MTI Instruments, Inc.). The span length of the beam was 9.8 mm. The displacement speed of the head was set to 0.05 mm/min. Specimen dimension was according to the ASTM standard (C1684-18). Based on the ASTM standard, the aspect ratio (length to width) of the test specimen should be more than three. For three-point bending tests, specimens were ~1 mm in diameter and ~15 mm in length.

**DSC Analysis.** The polymer-to-ceramic transformation was investigated by differential scanning calorimetry/thermal gravimetric analysis (DSC/TGA) performed using a STA449/F5 Netzsch instrument. The thermal analysis was performed from room temperature up to 1000 °C with a heating rate of 20 °C/min in a nitrogen gas environment.

**SEM Imaging.** A Zeiss Supra 40 SEM was utilized to observe the cross section of the ceramic specimens. Since a good electrical conductivity is required to obtain high-quality SEM images, a gold—palladium film was sputtered on the ceramic specimens. The composition of the pyrolyzed SiOC ceramic was measured by the EDAX material analysis system.

**Casting.** Since the precursor polymer was in the solution phase, a mold was used to prepare casting specimens. Molds were prepared by making several cylindrical holes in PTFE (poly(tetrafluoroethylene)), which can withstand high temperatures up to  $\sim\!200~^{\circ}\text{C}$  ( $\geq$  crosslinking temperature).

#### ASSOCIATED CONTENT

#### Supporting Information

The Supporting Information is available free of charge at https://pubs.acs.org/doi/10.1021/acsami.0c08260.

Printing duration of selected geometries; pyrolysis temperature—time profile; TGA response; 3D-printed beam under three-point bending test; SEM images; EDS spectra; EDS elemental analysis and composition; side-by-side images of a cured and pyrolyzed helix for shrinkage analysis after pyrolysis (PDF)

3D printing of airfoil, helix, and curved honeycomb structure (MP4)

#### AUTHOR INFORMATION

#### **Corresponding Author**

Majid Minary - Jolandan — Department of Mechanical Engineering, University of Texas at Dallas, Richardson, Texas 75080, United States; orcid.org/0000-0003-2472-302X; Email: majid.minary@utdallas.edu

#### **Authors**

Mohammadreza Mahmoudi — Department of Mechanical Engineering, University of Texas at Dallas, Richardson, Texas 75080, United States

Chao Wang — Department of Mechanical Engineering, University of Texas at Dallas, Richardson, Texas 75080, United States

Salvador Moreno — Department of Mechanical Engineering, University of Texas at Dallas, Richardson, Texas 75080, United States

Scott R. Burlison — Department of Mechanical Engineering, University of Texas at Dallas, Richardson, Texas 75080, United States

Diana Alatalo — Department of Mechanical Engineering, University of Texas at Dallas, Richardson, Texas 75080, United States

- Fatemeh Hassanipour Department of Mechanical Engineering, University of Texas at Dallas, Richardson, Texas 75080, United States
- Samantha E. Smith Department of Mechanical Engineering, University of Texas at Dallas, Richardson, Texas 75080, United States
- Mohammad Naraghi Department of Aerospace Engineering, Texas A&M University, College Station, Texas 77843, United States; Occid.org/0000-0002-1841-7598

Complete contact information is available at: https://pubs.acs.org/10.1021/acsami.0c08260

#### **Author Contributions**

M.M.-J. designed the research. M.M., C.W., S.M., and S.R.B. carried the majority of the experimental work. D.A. and F.H. helped with the rheology experiments and data analysis. S.E.S. and S.R.B. carried our part of the preliminary work. M.N. participated in the design of work and data analysis. All authors contributed to the writing and editing of the manuscript.

#### **Notes**

The authors declare no competing financial interest.

#### ACKNOWLEDGMENTS

This work is supported by the National Science Foundation (CMMI, Award #1930621), and The Eugene McDermott Professorships at UT Dallas. The rheometer used in this work was acquired thourgh NSF grant CBET-1707063.

#### REFERENCES

- (1) Chen, Z.; Li, Z.; Li, J.; Liu, C.; Lao, C.; Fu, Y.; Liu, C.; Li, Y.; Wang, P.; He, Y. 3d Printing of Ceramics: A Review. *J. Eur. Ceram. Soc.* **2019**, *39*, 661–687.
- (2) Zocca, A.; Colombo, P.; Gomes, C. M.; Günster, J. Additive Manufacturing of Ceramics: Issues, Potentialities, and Opportunities. *J. Am. Ceram. Soc.* **2015**, *98*, 1983–2001.
- (3) Griffith, M. L.; Halloran, J. W. Freeform Fabrication of Ceramics Via Stereolithography. *J. Am. Ceram. Soc.* **1996**, *79*, 2601–2608.
- (4) Chartier, T.; Chaput, C.; Doreau, F.; Loiseau, M. Stereolithography of Structural Complex Ceramic Parts. *J. Mater. Sci.* **2002**, 37, 3141–3147.
- (5) Lv, X.; Ye, F.; Cheng, L.; Fan, S.; Liu, Y. Binder Jetting of Ceramics: Powders, Binders, Printing Parameters, Equipment, and Post-Treatment. *Ceram. Int.* **2019**, *45*, 12609–12624.
- (6) Bertrand, P.; Bayle, F.; Combe, C.; Goeuriot, P.; Smurov, I. Ceramic Components Manufacturing by Selective Laser Sintering. *Appl. Surf. Sci.* **2007**, 254, 989–992.
- (7) Shahzad, K.; Deckers, J.; Kruth, J.-P.; Vleugels, J. Additive Manufacturing of Alumina Parts by Indirect Selective Laser Sintering and Post Processing. *J. Mater. Process. Technol.* **2013**, 213, 1484–1494.
- (8) Franchin, G.; Wahl, L.; Colombo, P. Direct Ink Writing of Ceramic Matrix Composite Structures. J. Am. Ceram. Soc. 2017, 100, 4397–4401.
- (9) Colombo, P.; Mera, G.; Riedel, R.; Sorarù, G. D. Polymer-Derived Ceramics: 40 Years of Research and Innovation in Advanced Ceramics. *J. Am. Ceram. Soc.* **2010**, *93*, 1805–1837.
- (10) Pham, T. A.; Kim, D. P.; Lim, T. W.; Park, S. H.; Yang, D. Y.; Lee, K. S. Three-Dimensional Sicn Ceramic Microstructures Via Nano-Stereolithography of Inorganic Polymer Photoresists. *Adv. Funct. Mater.* **2006**, *16*, 1235–1241.
- (11) Martínez-Crespiera, S.; Ionescu, E.; Kleebe, H.-J.; Riedel, R. Pressureless Synthesis of Fully Dense and Crack-Free Sioc Bulk Ceramics Via Photo-Crosslinking and Pyrolysis of a Polysiloxane. *J. Eur. Ceram. Soc.* **2011**, *31*, 913–919.

- (12) Shah, S. R.; Raj, R. Mechanical Properties of a Fully Dense Polymer Derived Ceramic Made by a Novel Pressure Casting Process. *Acta Mater.* **2002**, *50*, 4093–4103.
- (13) Zanchetta, E.; Cattaldo, M.; Franchin, G.; Schwentenwein, M.; Homa, J.; Brusatin, G.; Colombo, P. Stereolithography of Sioc Ceramic Microcomponents. *Adv. Mater.* **2016**, *28*, 370–376.
- (14) Schwentenwein, M.; Homa, J. Additive Manufacturing of Dense Alumina Ceramics. *Int. J. Appl. Ceram. Technol.* **2015**, *12*, 1–7.
- (15) Eckel, Z. C.; Zhou, C.; Martin, J. H.; Jacobsen, A. J.; Carter, W. B.; Schaedler, T. A. Additive Manufacturing of Polymer-Derived Ceramics. *Science* **2016**, *351*, 58–62.
- (16) Brigo, L.; Schmidt, J. E. M.; Gandin, A.; Michieli, N.; Colombo, P.; Brusatin, G. 3d Nanofabrication of Sioc Ceramic Structures. *Adv. Sci.* **2018**, *5*, No. 1800937.
- (17) Hinton, T. J.; Jallerat, Q.; Palchesko, R. N.; Park, J. H.; Grodzicki, M. S.; Shue, H.-J.; Ramadan, M. H.; Hudson, A. R.; Feinberg, A. W. Three-Dimensional Printing of Complex Biological Structures by Freeform Reversible Embedding of Suspended Hydrogels. *Sci. Adv.* 2015, 1, No. e1500758.
- (18) O'Bryan, C. S.; Bhattacharjee, T.; Hart, S.; Kabb, C. P.; Schulze, K. D.; Chilakala, I.; Sumerlin, B. S.; Sawyer, W. G.; Angelini, T. E. Self-Assembled Micro-Organogels for 3d Printing Silicone Structures. *Sci. Adv.* **2017**, 3, No. e1602800.
- (19) Bhattacharjee, T.; Zehnder, S. M.; Rowe, K. G.; Jain, S.; Nixon, R. M.; Sawyer, W. G.; Angelini, T. E. Writing in the Granular Gel Medium. *Sci. Adv.* **2015**, *1*, No. e1500655.
- (20) Lindahl, J.; Hassen, A.; Romberg, S.; Hedger, B.; Hedger, P., Jr; Walch, M.; DeLuca, T.; Morrison, W.; Kim, P.; Roschli, A.; Nuttall, D.; Czachowski, J.; Post, B.; Love, L.; Kunc, V. Large-Scale Additive Manufacturing with Reactive Polymers 2018.
- (21) O'Bryan, C. S.; Bhattacharjee, T.; Niemi, S. R.; Balachandar, S.; Baldwin, N.; Ellison, S. T.; Taylor, C. R.; Sawyer, W. G.; Angelini, T. E. Three-Dimensional Printing with Sacrificial Materials for Soft Matter Manufacturing. *MRS Bull.* **2017**, *42*, 571–577.
- (22) Li, J.; Lu, K.; Lin, T.; Shen, F. Preparation of Micro-/Mesoporous Sioc Bulk Ceramics. J. Am. Ceram. Soc. 2015, 98, 1753–1761.
- (23) Ionescu, E.; Kleebe, H. J.; Riedel, R. Silicon-Containing Polymer-Derived Ceramic Nanocomposites (Pdc-Ncs): Preparative Approaches and Properties. *Chem. Soc. Rev.* **2012**, *41*, 5032–5052.
- (24) Li, J. K.; Lu, K.; Lin, T. S.; Shen, F. Y. Preparation of Micro-/Mesoporous Sioc Bulk Ceramics. *J. Am. Ceram. Soc.* **2015**, 98, 1753–1761.
- (25) Kulkarni, A.; Soraru, G.; Pearce, J. Polymer-Derived Sioc Replica of Material Extrusion-Based 3-D Printed Plastics. *Addit. Manuf.* **2020**, 32, No. 100988.
- (26) Jiang, H.; Wang, X.-H.; Lei, W.; Fan, G.-F.; Lu, W.-Z. Effects of Two-Step Sintering on Thermal and Mechanical Properties of Aluminum Nitride Ceramics by Impedance Spectroscopy Analysis. *J. Eur. Ceram. Soc.* **2019**, 39, 249–254.
- (27) Tian, X.; Yan, K.; Liu, H.; Zhao, J.; Yang, J. Effect of Co on Thermal and Mechanical Properties of Si3n4 Based Ceramic Tool Material. *Ceram. Int.* **2019**, *45*, 19435–19441.
- (28) Yuan, Q.; Chai, Z. F.; Huang, Z. R.; Huang, Q. A New Precursor of Liquid and Curable Polysiloxane for Highly Cost-Efficient Sioc-Based Composites. *Ceram. Int.* **2019**, *45*, 7044–7048.
- (29) ASTMStandard Test Method for Flexural Strength of Advanced Ceramics at Ambient Temperature—Cylindrical Rod Strength. In *C1684-18*; American Society of Testing Material, 2019.
- (30) ASTMStandard Practice for Reporting Uniaxial Strength Data and Estimating Weibull Distribution Parameters for Advanced Ceramics. In C1239-13; American Society of Testing Materials, 2018.
- (31) Khalili, A.; Kromp, K. Statistical Properties of Weibull Estimators. *J. Mater. Sci.* **1991**, *26*, 6741–6752.
- (32) Quinn, J. B.; Quinn, G. D. A Practical and Systematic Review of Weibull Statistics for Reporting Strengths of Dental Materials. *Dent. Mater.* **2010**, *26*, 135–147.

### **Supporting Information**

# 3-Dimensional Printing of Ceramics through "Carving" a Gel and "Filling in" the Precursor Polymer

Mohammadreza Mahmoudi<sup>1</sup>, Chao Wang<sup>1</sup>, Salvador Moreno<sup>1</sup>, Scott R. Burlison<sup>1</sup>, Diana Alatalo<sup>1</sup>, Fatemeh Hassanipour<sup>1</sup>, Samantha E. Smith<sup>1</sup>, Mohammad Naraghi<sup>2</sup>, Majid Minary - Jolandan<sup>1\*</sup>

The printing duration of selected printed geometries are summarized in table S1.

**Table S1** Printing duration of selected geometries shows in Figure 2.

Geometry	Printing time (s)			
Small helix	8			
Large truss-beam structure	115			
Grid 2D	55			
Cone helix	28			
Vase	90			
Small truss-beam structure	30			
Grid 3D	55			

Figure S1 shows the pyrolysis temperature – time profile. The profile was obtained based on thermogravimetric analysis since the polymer precursor experiences two main mass losses during crosslinking and ceramization phases.

<sup>&</sup>lt;sup>1</sup> Department of Mechanical Engineering, University of Texas at Dallas, Richardson TX 75080

<sup>&</sup>lt;sup>2</sup> Department of Aerospace Engineering, Texas A&M University, College Station, TX 77843

<sup>\*</sup> Email: majid.minary@utdallas.edu

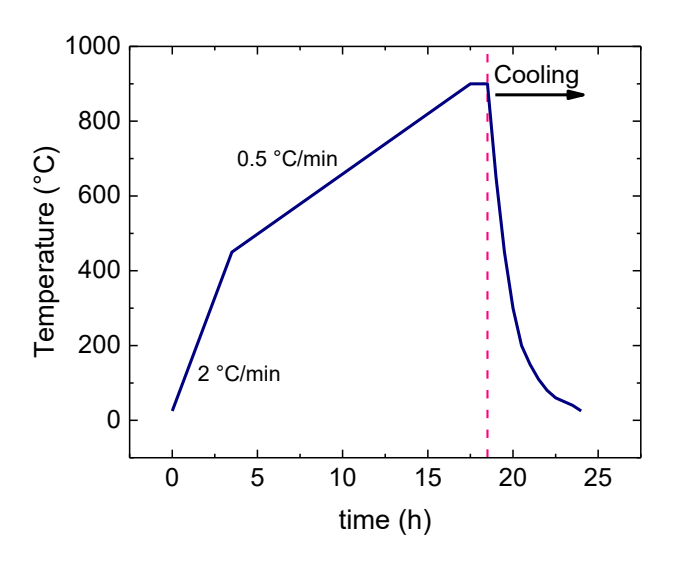


Figure S1 Pyrolysis temperature – time profile.

Figure S2 shows the TGA results for the support bath, cured casted-sample, and cured printed-sample. Cured here implies that the printed and cast samples were first cured and the thermal analysis was performed on the cured samples. This experiment was conducted to further understand the interaction between the support bath and the printed ceramic by considering the cast samples (free of support bath) as the control.

The support gel mass did not show significant change for temperature up to  $\sim 200$  °C, which shows that it is stable during curing process of the preceramic polymer at  $\sim 160$  °C. From 200 °C to 400 °C, there was a drastic change in the mass of the support bath, which corresponded to the mineral oil evaporation (boiling point  $\sim 310$  °C). The  $\sim 8$  wt. % remaining mass after heating to a temperature of 1000 °C corresponds to  $\sim 5$  wt. % silica nanoparticles in the bath composition and minor residues from mineral oil burning.

The cured-cast specimen does not show noticeable mass loss for temperature  $\sim 600$  °C. For higher temperature, up to 1000 °C, there is a total mass loss of  $\sim 11.5\%$ , which corresponds to ceramization. The cured-printed specimen shows an initial mass loss at similar temperature to the support bath, an indication that some residues of the support bath (mineral oil and silica nanoparticles) are left on the printed specimen after retrieval from the bath. The mineral oil part of this residue is evaporated in the process, leaving behind a coating of consolidated silica nanoparticles on the specimen. This is also confirmed by SEM images and EDS analysis in Figure S4 and Figure S5 and Table S2. The thickness of this coating was estimated to be  $\sim 115$  microns. For this estimation, a number of helices were printed and the mass of the extruded polymer was calculated based on the printing time and the flow rate in the nozzle. After curing, the mass of each printed-cured specimen was again measured. This was repeated for the pyrolyzed specimens. Given the density of the preceramic polymer solution (1.1 g/cm³) and the density of the mineral oil (0.85 g/cm³), the volume of the polymer and volume of the support bath residue was estimated, and the thickness of the oil coating on the cured sample was obtained.

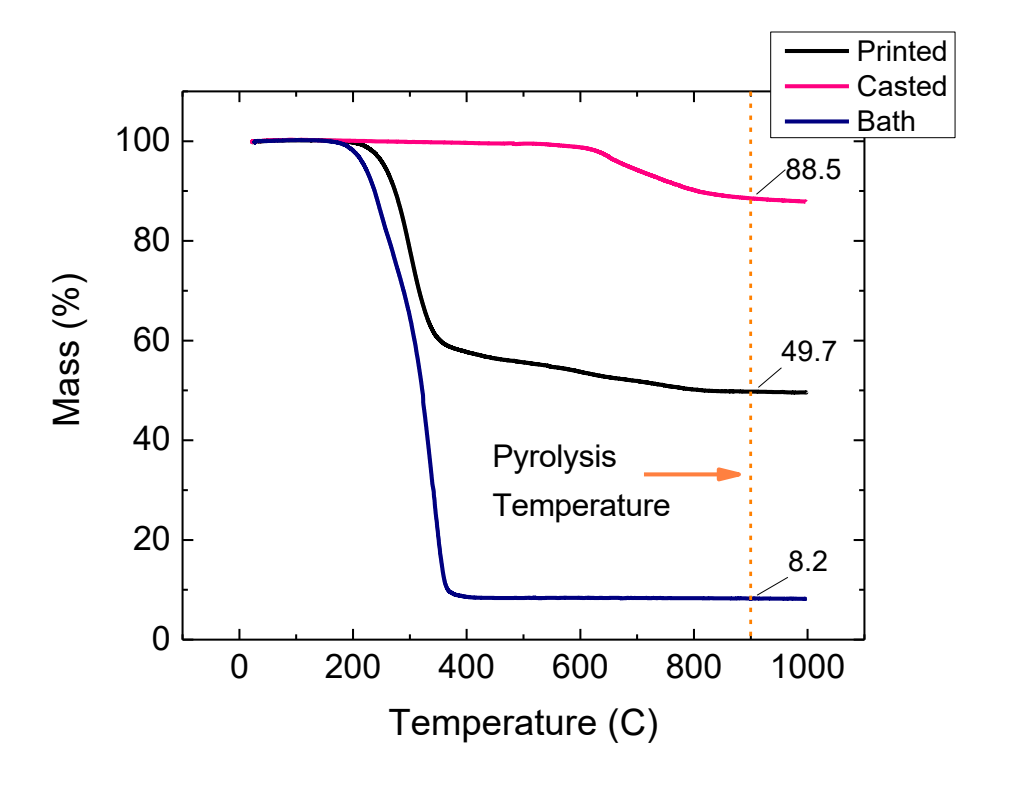


Figure S2 TGA response for the support bath, cross-linked cast material, and cross-linked printed-material.

Figure S4 shows SEM images of a 3D-printed specimen after three-point bending experiment. Figure S4A shows the two halves of the specimen after failure. Figure S4B-D show the surface and the cross-section of the specimen. The image of the cross-section shows that the specimen is dense, without any noticeable pores and cracks at SEM image resolution. The rough surface morphology can be attributed to the residual silica and oil burn-out on the specimen, as discussed above, and also revealed in the EDS spectra in Figure S4H. The gold and palladium peaks were because of the sputtering process needed to enhance the electrical conductivity of the specimen before SEM/EDS analysis. Figure S4A shows that the specimen failed on the tension-dominated side as expected for 3-point bending experiment. Magnified SEM images in figure 4S E-G show the brittle nature of the fracture with shiny and smooth surfaces covered with hackle lines radiating from the fracture origin.

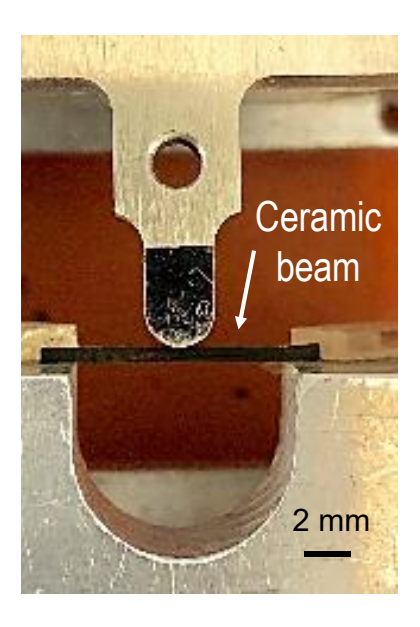
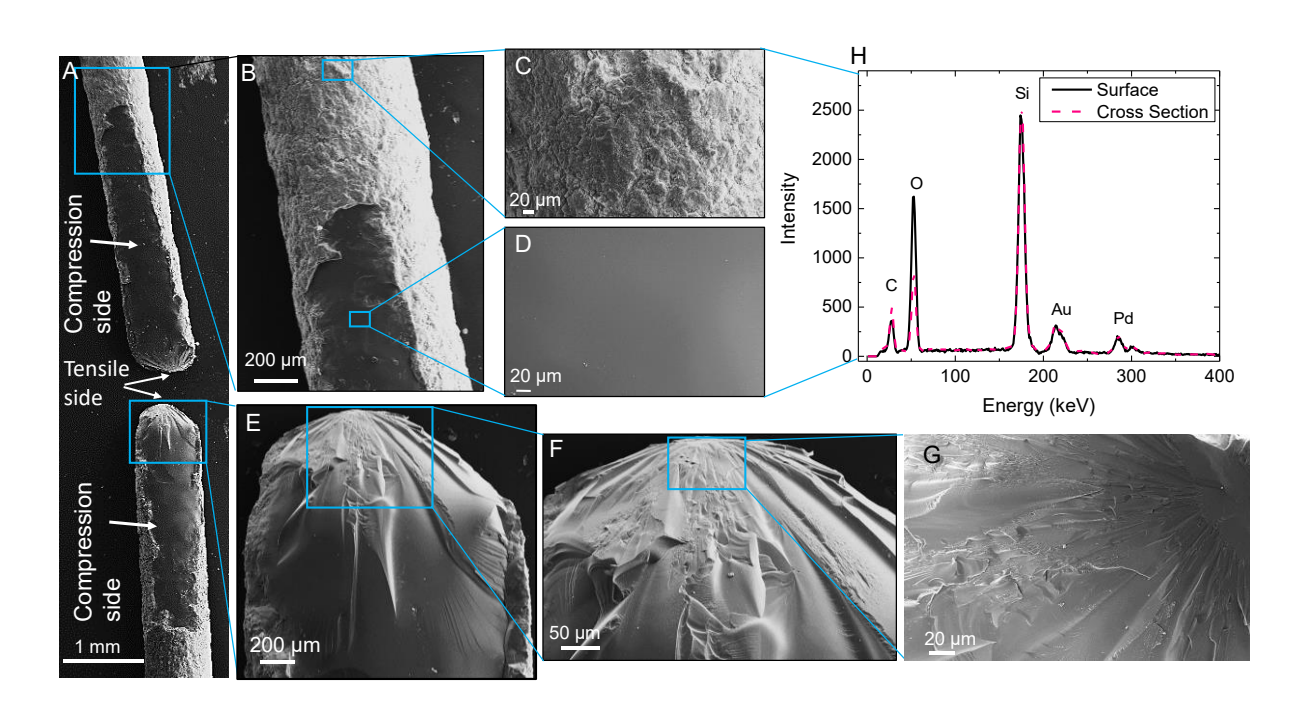


Figure S3. A 3D printed beam under 3-point bending test.



**Figure S4** (A) - (G) SEM images of the three-point bending specimen after failure. (H) EDS spectra acquired from the cross-section and surface of the specimen.

The approximate composition of the 3D-printed specimens was obtained from EDS spectra (Figure S5) and presented in Table S2. For comparison, EDS spectra of the cast specimens are also

presented. There is a minor difference in the elemental composition between the surface and cross-section of the cast specimen, which can be attributed to minor oxidation on the surface. The much larger oxygen content on the printed specimen surface is attributed to the residual silica nanoparticles, as discussed above.

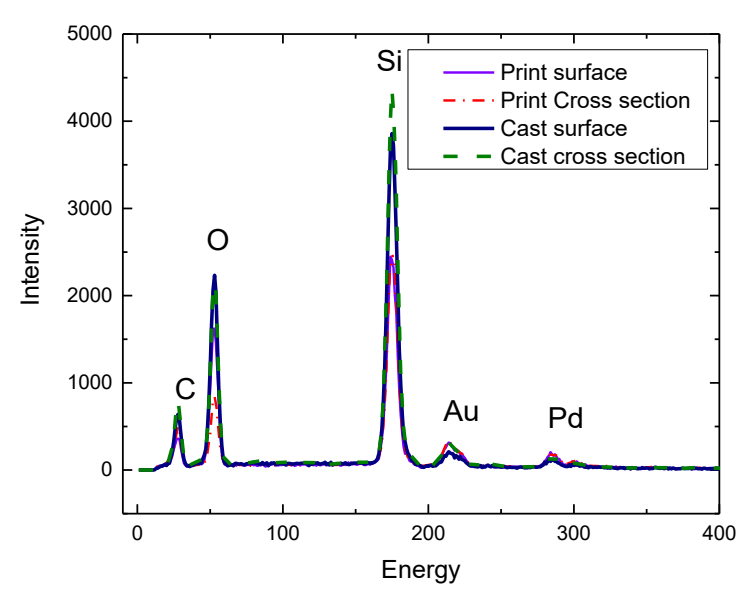


Figure S5 EDS spectra of surface and cross-section of both 3D-printed and cast ceramic.

**Table S2** EDS elemental analysis and composition for the cast and printed specimens.

Element (at. %)	С	0	Si	Au	Pd	Composition
Cast surface	35	48.04	16.12	0.47	0.37	SiO <sub>3</sub> C <sub>2.2</sub>
Print surface	32.17	54.59	11.80	0.77	0.68	$\mathrm{SiO}_{4.6}\mathrm{C}_{2.7}$
Cast cross-section	39.15	44.38	15.58	0.49	0.39	$\mathrm{SiO}_{2.8}\mathrm{C}_{2.5}$
Print cross-section	44.64	39.45	14.01	0.98	0.93	SiO <sub>2.8</sub> C <sub>3.18</sub>

Figure S6 shows side-by-side images of cross-linked and pyrolyzed specimens. The linear shrinkage (difference in the diameter d) was estimated to be ~15%. The shrinkage value was obtained using image analysis by subtracting the thickness of the residual oil. The 3D printed PDC had the

ceramic yield  $\sim$  84%. Using this data, the ratio of the density of the pyrolyzed to the cured ceramic was obtained as following:

$$\frac{\rho_{pyrolyzed}}{\rho_{cured}} = \frac{\left(\frac{m}{v}\right)_{pyrolyzed}}{\left(\frac{m}{v}\right)_{cured}} = \frac{\frac{0.84 \text{ m}}{(1 - linear \, shrinkage)^3}}{\frac{m}{v}} = \frac{\frac{0.84 \text{ m}}{0.85^3 \text{ v}}}{\frac{m}{v}} = 1.37$$

Given the density of the preceramic polymer solution (1.1 g/cm $^3$ ), the final density of the pyrolyzed ceramic is estimated to be  $\sim 1.6$  g/cm $^3$ .

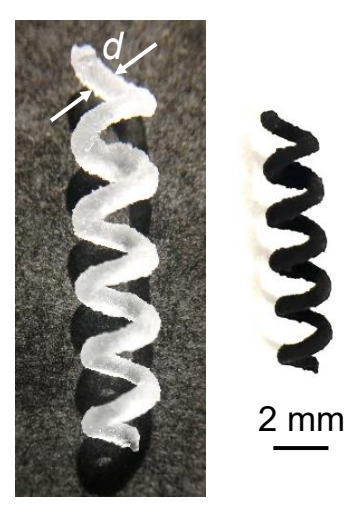


Figure S6 Side-by-side images of a cured and pyrolyzed helix for shrinkage analysis after pyrolysis.